


Anti-Poiseuille flow: Increased vortex velocity at superconductor edgesT. Okugawa ^{1,2}, A. Benyamini ³, A. J. Millis ^{3,4} and D. M. Kennes ^{1,2,5,*}¹*Institut für Theorie der Statistischen Physik, RWTH Aachen, 52056 Aachen, Germany*²*JARA -Fundamentals of Future Information Technology, 52056 Aachen, Germany*³*Department of Physics, Columbia University, New York, New York 10027, USA*⁴*Center for Computational Quantum Physics, Flatiron Institute, 162 5th Avenue, New York, New York 10010, USA*⁵*Max Planck Institute for the Structure and Dynamics of Matter, Center for Free Electron Laser Science, Luruper Chaussee 149, 22761 Hamburg, Germany* (Received 24 December 2021; revised 27 April 2022; accepted 27 May 2022; published 22 June 2022)

Using the time-dependent Ginzburg-Landau equations, we study vortex motion driven by an applied current in two-dimensional superconductors in the presence of a physical boundary. At smaller sourced currents the vortex lattice moves as a whole, with each vortex moving at the same velocity. At the larger sourced current, the vortex motion is organized into channels, with vortices in channels closer to the sample edges moving faster than those farther away from sample edges, opposite the Poiseuille flow of basic hydrodynamics in which the velocity is lowest at the boundaries. At intermediate currents, a stick-slip motion of the vortex lattice occurs in which vortices in the channel at the boundary break free from the Abrikosov lattice, accelerate, move past their neighbors, and then slow down and reattach to the vortex lattice, at which point the stick-slip process starts over. These effects could be observed experimentally, e.g., using fast scanning microscopy techniques.

DOI: [10.1103/PhysRevB.105.224512](https://doi.org/10.1103/PhysRevB.105.224512)**I. INTRODUCTION**

In the presence of an applied magnetic field a type-II superconductor may exhibit a vortex state, characterized by a certain density of order parameter singularities (vortices). In equilibrium and in the absence of important disorder effects, the vortices generically form an ordered “Abrikosov lattice” [1]. An applied current produces a force on the vortices, and the resulting vortex motion leads to dissipation [1–3], which is one of the main concerns for many applications such as superconducting qubits and superconducting digital memory [4,5], high-field magnets [6], terahertz radiation sources [7], and resonant cavities in particle accelerators [8,9]. A deeper understanding of the nature of vortex motion may enhance device performance, enabling many intriguing applications [10–13].

Vortex structures driven by an external current in systems with [14–21] and without [22–26] pinning sites have been studied. Similarly, some recent works on skyrmion dynamics in magnetic systems, which have many similarities to the vortices in a type-II superconductor, have attracted attention [27,28]. Vortex dynamics is even richer in the presence of specific geometrical features [29–33]. In particular, intricate inhomogeneous flow patterns are observed near boundaries in vortex arrays [31], colloidal bubbles [34], and ion crystals [35]. Of particular interest is the “phase slip line state” [36–38] in which a set of parallel vortex rows is created and each vortex follows in its own “assigned” channel. This phenomenon originates from an effective attraction to the other vortices due to suppression of the order parameter created behind each moving vortex [39–41]. This mechanism was

analyzed in the context of the viscosity and the instability of the vortex motion using both Bardeen-Stephen and Larkin-Ovchinnikov theories [2,24,42].

In this work, we use time-dependent Ginzburg-Landau (TDGL) theory [43–45] to investigate the flux flow properties of clean two-dimensional superconductors driven by externally sourced currents in finite geometries. We find a low-current regime in which the vortex lattice moves as a whole, a high-current “anti-Poiseuille” regime in which vortices near the sample boundaries move faster, and an intermediate regime characterized by a “stick-slip” behavior. We show that our results can be understood in terms of a Bardeen-Stephen [2] analysis in which the reduced order parameter close to the edge provides a lower viscosity for the vortex motion and can be understood in terms of the phase slip line state.

The rest of this paper is organized as follows. In Sec. II, we present our model and the computational method adopted for this paper. In Secs. III and IV, we show the main results of our calculations and the corresponding discussion, respectively. Finally, Sec. V concludes the paper with a summary of results and discussion of future work.

II. FORMALISM

We use TDGL equations to describe the dynamics of a complex superconducting order parameter $\Delta = |\Delta|e^{i\phi}$ in a two-dimensional strip geometry in the presence of both an external current created by a source and drain of particles whose strength is denoted by Q and an external magnetic field \mathbf{B} directed perpendicular to the superconducting film. The electromagnetic field is expressed by the vector potential \mathbf{A} and the scalar potential Θ . We denote the charge density

*Dante.Kennes@rwth-aachen.de

as ρ and current density as \mathbf{J} and choose the units to be $\hbar = c = e = 1$. The equations are [3,46–48]

$$\frac{1}{D}(\partial_t + 2i\Psi)\Delta = \frac{1}{\xi^2\beta}\Delta[\alpha - \beta|\Delta|^2] + [\nabla - 2i\mathbf{A}]^2\Delta, \quad (1)$$

$$\mathbf{J} = \sigma[-\nabla\Psi - \partial_t\mathbf{A}] + \sigma\tau_s\text{Re}[\Delta^*(-i\nabla - 2\mathbf{A})\Delta], \quad (2)$$

$$\rho = \frac{\Psi - \Theta}{4\pi\lambda_{TF}^2}, \quad (3)$$

$$\partial_t\rho + \nabla \cdot \mathbf{J} = Q, \quad (4)$$

$$\nabla^2\Theta = -4\pi\rho. \quad (5)$$

Here D is the normal state diffusion constant, Ψ is the electrochemical potential per electron charge, $\xi = \sqrt{6D/\tau_s}$, and the superconducting coherent length is given as $\xi_0 = \xi/\sqrt{\alpha/\beta}$, where τ_s is the spin-flip scattering time. α and β are system-dependent constants, which set the magnitude of the order parameter. σ and λ_{TF} are the normal state conductivity and the Thomas-Fermi static charge screening length, respectively. We measure length in units of ξ and time in units of ξ^2/D (since ξ is the unit of length, we write this as D^{-1}). We choose the parameters as follows: $\alpha = \beta = 1$, $\tau_s = 6D/\xi^2$, $\lambda_{TF}/\xi = 1$, and $\sigma/(D/\xi^2) = 1$, and we set the length and width of the two-dimensional (2D) strip to be $L = 50\xi$. We confirmed that this particular parameter choice does not affect the general conclusions of this paper. We choose the Coulomb gauge $\nabla \cdot \mathbf{A} = 0$ [49].

We study a system that is periodic in y and has an open superconductor-vacuum boundary conditions in x [24,50,51]:

$$\Delta(y + L) = \Delta(y), \quad (6)$$

$$(-i\nabla_x - A_x)\Delta|_{x=0, L} = 0, \quad (7)$$

$$[-(\nabla\Psi)_x - \partial_t A_x]|_{x=0, L} = 0. \quad (8)$$

The advantage of the periodic boundary condition is that it avoids the need to consider complications, which are irrelevant here, related to the creation and destruction of vortices at sample edges [52].

We consider very thin films in which the sample thickness is much less than the London penetration depth, so that the magnetic field can be taken to be spatially uniform and described by the Coulomb-gauge vector potential $\mathbf{A} = (0, B(x - L/2), 0)$. We choose magnetic field values such that the number of vortices is commensurate with the system size so that each vertical line of vortices in Fig. 1 has the same number of vortices to avoid additional complications that arise when there is an additional vortex which could go into any one of the channels.

The external current is introduced by the source term Q in Eq. (4), which defines source and drain regions of width ξ over the entire length of the open boundaries. Specifically, we take Q to be independent of y and $Q(x, y) \neq 0$ only for $0 < x < \xi$ and $L - \xi < x < L$. Thus, this current flow is homogeneous in the entire sample (except for the source and drain sections).

The simulations were performed using a finite-element method in space implemented in FENICS [54], and we discretize the time derivative by a finite-difference approximation

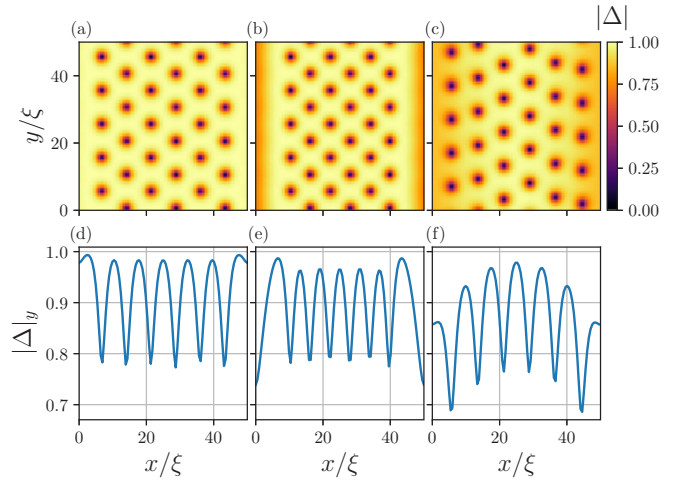


FIG. 1. False-color representation of the magnitude of the superconducting order parameter $|\Delta|$ (top) and the corresponding y -averaged order parameter, denoted as $|\Delta|_y$, against x (bottom) for zero applied current [$Q/(D^2/\xi^6) = 0$] in (a), (b), (d), and (e) and nonzero applied current [$Q/(D^2/\xi^6) = 0.55$] in (c) and (f). The magnetic field strengths are $\xi^2 B = 0.043$ for (a), (c), (d), and (f) and $\xi^2 B = 0.053$ for (b) and (e). The configuration depicted in (c) is a snapshot showing one instance in time of a dynamic state. The corresponding video is available in the Supplemental Material (SM) as Video 14 [53].

in which the order parameter is updated in time steps of $D\Delta t = 0.5$. We have verified that decreasing the time step does not change the results. The initial conditions (at time $t = 0$) of all variables except Δ are set to zero, while $\Delta(x, y, t = 0)$ is chosen to describe the superconducting state with some random fluctuation over the entire 2D sample [55].

In our calculation protocol we first set the current to zero and evolve the system; once a stable vortex lattice is formed, we introduce the current and then analyze the flow after a steady state is reached. To be specific, nonzero Q is introduced at $Dt = 1000$, when a rigid vortex structure has already been formed, and an analysis of vortex flow created by the sourced current is performed after $Dt = 1500$.

III. RESULTS

In this section we present the main features of our results. Before doing so we summarize the expected physics. In a magnetic field, the superconducting order parameter of a thin film exhibits vortices, points at which the order parameter vanishes and around which there is a quantized circulation of the superconducting phase. The density of vortices is set by the applied field, and the energy associated with superposing the quantized circulations leads to vortex-vortex interactions that are repulsive and logarithmic at long scales; the resulting equilibrium configuration is a triangular “Abrikosov lattice” with the lattice vectors parallel or at angles of $\pm\pi/3$ to the open boundaries at $x = 0, L$ [shown in Fig. 1(a) as an example]. In this state, if the order parameter amplitude is averaged over y and then plotted against x , vortex rows corresponding to equally spaced minima in the order parameter amplitude are evident [shown in Fig. 1(d) as an example]. In

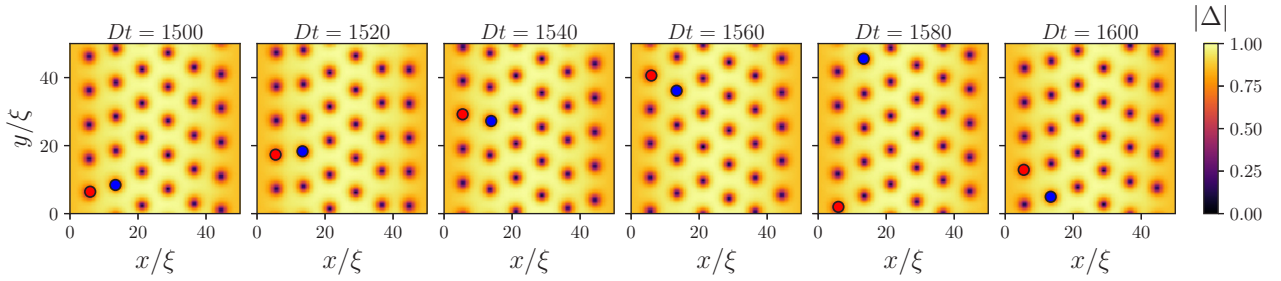


FIG. 2. Series of false-color plots of the magnitude of the order parameter $|\Delta|$ for $\xi^2 B = 0.043$ and $Q/(D^2/\xi^6) = 0.55$ at different times. The same two vortices are labeled by red and blue dots for each time to highlight that the vortices close to the edge (red dot) move faster than the ones in the bulk (blue dot). Each plot is a snapshot showing instances in time which are separated by $20D^{-1}$ from left to right, and the initial time is $Dt = 1500$. The corresponding video is available in the SM as Video 14 [53].

the presence of an applied current \mathbf{J} a vortex is accelerated by a Lorentz force $\mathbf{F} = \mathbf{J} \times \mathbf{B}/c$ directed perpendicular to the current and the magnetic field and experiences a viscosity η , which is within Bardeen-Stephen picture given by [3]

$$\eta = \Phi_0 \sigma \frac{H_{c2}}{c^2} \sim \Delta^2, \quad (9)$$

where σ is the conductivity appearing in the TDGL equations and Φ_0 is the flux quantum. H_{c2} is the upper critical field which is proportional to the square of the superconducting order parameter in the clean limit studied here. The system we study has a translation invariance in the y direction so that in the presence of a current one possible solution is a uniformly translating vortex lattice in which the velocity is determined from the Lorentz force and the viscosity. As we shall see, in our system, other solutions are possible, corresponding to nonuniform vortex motion. In all of our investigations, the nonuniformly moving state exhibits the same row structure as in the equilibrium and uniformly moving states, but vortices in different rows may move with different velocities.

A. Equilibrium

First, we perform simulations without an externally sourced current, $Q = 0$. We initialize our simulation as described in Sec. II and allow the system to evolve to a time-independent state. The time evolution takes around $600D^{-1}$. Figure 1(a) presents a false-color plot of the magnitude of the order parameter $|\Delta|$ against the x - y position in our sample for a magnetic field of $B = 0.043\xi^2$. As expected, an Abrikosov vortex lattice is formed, with the lattice aligned with the boundaries. The periodic boundary conditions along y mean that there is a continuous family of equilibrium solutions translated by arbitrary amounts along y . The vortex positions are visible as regions of very small order parameter amplitude, and the row structure alluded to above is evident. From Fig. 1(d), which plots $|\Delta|_y$, the y average of the order parameter in Fig. 1(a) as a function of x , we see essentially no boundary effects, except for a small enhancement near the sample edges related to a weak tendency for vortices to avoid the edges because of supercurrent reflection at the boundary.

Figures 1(b) and 1(e) show similar plots obtained for the slightly larger magnetic field $B = 0.053/\xi^2$. In this case the time to equilibration is rather shorter: $100D^{-1}$ [initialized from the state shown in Figs. 1(a) and 1(d)], and despite

the larger field, new vortices are not induced in the sample. Instead, the vortex lattice pulls farther away from the sample edges, leading to a higher vortex density in the sample center, while the order parameter near the sample edges is strongly suppressed. The stronger suppression of the order parameter at the boundary signals the incipient formation of a new row of vortices which would take place at even higher fields.

B. Nonzero current drive

A current applied in the x direction will cause the vortex lattice to move in the y direction. Because our model has no pinning, vortices will move under any applied current. At small applied currents our numerically computed solution is just a uniformly translating vortex lattice. However, above a critical current the lattice structure is somewhat disrupted. The parallel chain structure remains, but the vortices in the chain closest to the sample edge flow at a higher velocity. This is illustrated in Fig. 2, which shows a series of false-color plots of the order parameter amplitude presented at time intervals $20D^{-1}$ apart. Two vortices, one in the leftmost row and one in the second row from the left, are highlighted by red and blue dots, respectively. The difference in velocities is evident.

To quantify the dependence of the differential vortex velocity on the magnitude of the source term Q in Eq. (4), we present in Fig. 3 a plot of the difference of the time-averaged velocities of two tagged particles, v_1 of a vortex in the leftmost row and v_2 of a vortex in the adjacent row (e.g., the red and blue vortices in Fig. 2, respectively) as a function of Q . We see that the difference in velocities remains zero up to a critical value $Q \approx 0.4D^2/\xi^6$. For larger Q the time-averaged velocity difference increases linearly with $Q - Q_c$ until, at a yet larger $Q \approx 0.6D^2/\xi^6$, the system is reset: the number of vortex channels changes from six to four due to strong suppression of the order parameter close to the open boundary (see the Supplemental Material (SM), Videos 17, 18, and 19 [53]). In the newly established four-channel structure, the same characteristic as for the intermediate regime $0.4 < Q/(D^2/\xi^6) < 0.6$ is observed, as shown in Fig. 3 by a linear increase as a function of $Q/(D^2/\xi^6)$ after the jump in the curve.

IV. INTERPRETATION

We now argue that the velocity differential arises from a position dependence of the viscosity. We see from Figs. 1(c)

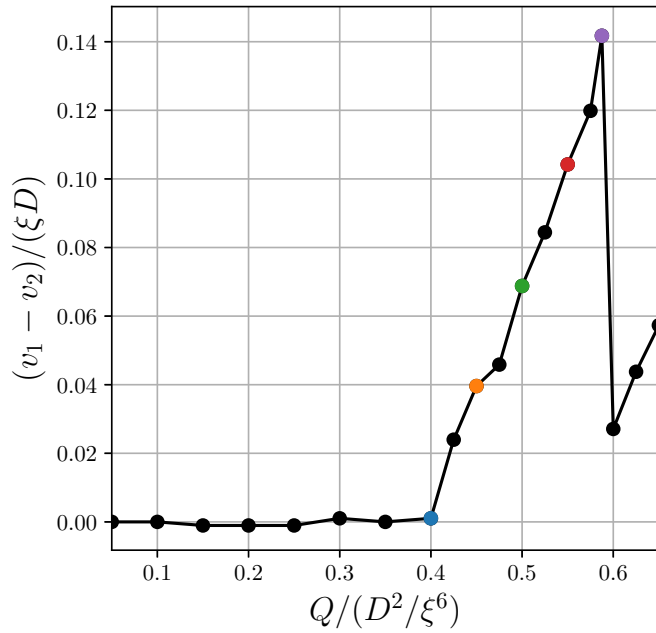


FIG. 3. Differences of the time-averaged velocities of two tagged particles, v_1 of a vortex in the leftmost row and v_2 of a vortex in the adjacent row (e.g., the red and blue vortices in Fig. 2, respectively), as a function of the strength of the source term Q (a plot for the individual v_1 and v_2 as a function of Q is shown in Fig. 8 in Appendix A). The vortex speeds are extracted from the simulations averaging from $Dt = 1500$ to $Dt = 1980$. The color corresponds to the parameters shown in Fig. 7. All corresponding videos are available in the SM [53] (see also Table I in Appendix B).

and 1(f) that at high drive current the typical value of $|\Delta|$, $|\Delta|_y$, far from a vortex is smaller near the sample edge than in the middle, implying via Eq. (9) that the vortices closest to the sample edge experience a lower viscosity. As clearly seen from the comparison between Figs. 1(d) and 1(f), in the presence of an externally sourced current, $|\Delta|_y$ in the region away from the vortices is reduced as it goes to the sample edge. To study the dependence of the reduction of the order parameter on the strength of the source term Q in Eq. (4), we define the time- and y -direction-averaged order parameter amplitude, denoted as $|\bar{\Delta}|$ in each vortex row, and plot in Fig. 4 the ratio of $|\bar{\Delta}|$ assigned in the two rows, $|\bar{\Delta}|_1$ in the leftmost row and $|\bar{\Delta}|_3$ in the middle left row. The ratio $|\bar{\Delta}|_1/|\bar{\Delta}|_3$ monotonously decreases both before and after $Q \approx 0.6D^2/\xi^6$, where the number of vortex channels changes from six to four, which implies that the viscosity difference between the leftmost and middle left rows increases as the sourced current increases within the systems with the same number of vortex channels.

Now let us consider the equation of motion in the y direction for a vortex in the leftmost row, supposing that the other vortices in the system are in an ordered, uniformly translating, state:

$$F_{VL}(y) + \frac{J\Phi_0}{c} = \eta_1 \dot{y}. \quad (10)$$

Here F_{VL} is the force arising from all of the other vortices. The current term may be related to the velocity of the uniformly translating part of the vortex lattice, denoted V , as $\frac{J\Phi_0}{c} = \bar{\eta}V$,

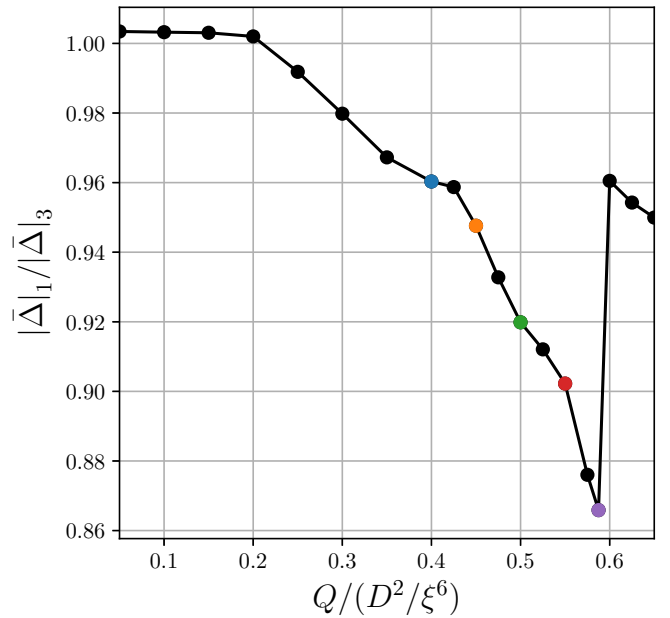


FIG. 4. Ratio of the averaged order parameter amplitude between $|\bar{\Delta}|_1$ in the leftmost row (edge) and $|\bar{\Delta}|_3$ in the middle left row (bulk) as a function of the strength of the source term Q . The x -dependent order parameter $|\bar{\Delta}|$ is calculated by averaging over the y direction and over the same time duration as for the vortex speed shown in Fig. 3. The color corresponds to the parameters shown in Fig. 7. All corresponding videos are available in the SM [53] (see also Table I in Appendix B).

where $\bar{\eta}$ is the average viscosity relevant to these vortices. In the frame comoving with the uniformly translating state Eq. (10) becomes

$$F_{VL}(y) + (\bar{\eta} - \eta_1)V = \eta_1 \dot{y}. \quad (11)$$

In other words, in the comoving frame the vortices at the edge of the sample experience two forces: one set by the mean velocity and the viscosity difference and one from the lattice of uniformly moving vortices. This latter force is periodic under translation by the vortex lattice vector and has a maximum value. At small current, both the difference in viscosity and the mean velocity are small, so this force is insufficient to overcome the force from the vortex lattice. The solution in the comoving frame is then $y = 0$, with y shifted from its equilibrium position by an amount proportional to the force. As the current is increased, the $(\bar{\eta} - \eta_1)V$ term increases, the shift in mean position increases, and when the position exceeds the point of maximum lattice force, the solution in the comoving frame becomes time dependent.

A. Anti-Poiseuille flow

As discussed above, in the nonuniformly moving state [$0.4 < Q/(D^2/\xi^6)$ in Fig. 7 below], the vortices move faster at the edge of the sample because the vortices closest to the edge experience a lower viscosity due to the reduction of the order parameter, shown in Eq. (9). To quantify the relation between the vortex velocity and the reduction of the order parameter, here we perform a simple analysis by neglecting vortex-vortex interaction and the corresponding force arising

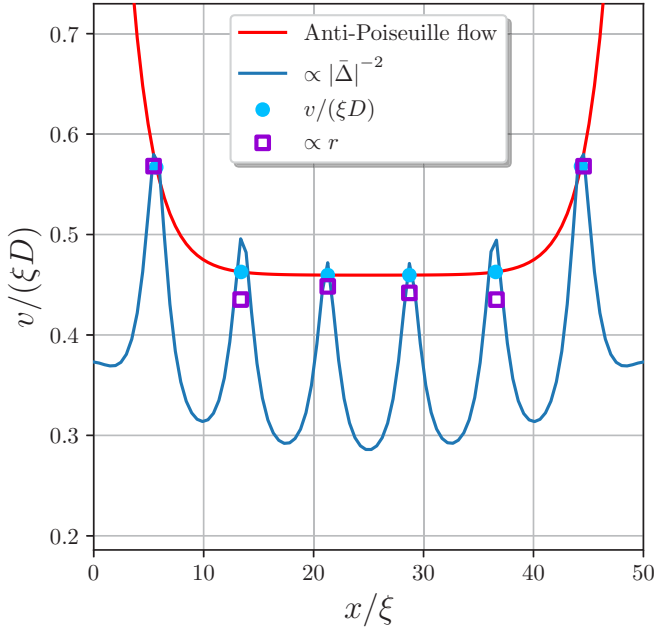


FIG. 5. Average speed of the vortex flow depending on its spatial position along x . The same averaging procedures as in Figs. 3 and 4 are used for the vortex speed v and the x -dependent order parameter $|\bar{\Delta}|$, respectively. To obtain a quantification of anti-Poiseuille flow, we fit the vortex speeds by $C_0 + C_1 \cosh[C_2(x - L/2)/\xi]$, yielding $C_0 = 0.456$, $C_1 = 3.32 \times 10^{-5}$, and $C_2 = 0.455$. The resistance over the separate channels $r = \Delta\bar{\Theta}$ is calculated by taking the differences of the averaged scalar potential $\bar{\Theta}$ between each vortex channel (see Fig. 6 for details), where $\bar{\Theta}$ is obtained from the same averaging procedure as for $|\bar{\Delta}|$. The same parameters as in Fig. 2 are chosen for the simulation.

from it, $F_{VL} \approx 0$, which enables us to consider the dynamics of each vortex row independently and may be reasonable in the large-current regime in our present study. In this case, Eq. (10) can be applied to all vortex rows, which is given as $J_{\frac{\Phi_0}{c}} = \eta\dot{y}$. Since the current J is homogeneous over almost the entire two-dimensional sample in our simulations (except the source and drain sections), together with Eq. (9), we can get a simple prediction for the vortex speed and the order parameter:

$$\dot{y} \propto \Delta^{-2}. \quad (12)$$

In order to check relation (12), we summarize representative results in Fig. 5, where we plot time-averaged vortex speeds v (for an analysis of the time-dependent velocity \dot{y} , see Sec. IV C) and the x -dependent inverse of the square of the averaged order parameter $|\bar{\Delta}|^{-2}$. Overall, we find good agreement between the simple prediction (12) and the full numerical simulations for v . The slight disagreement between $v/(\xi D)$ (blue dots) and $|\bar{\Delta}|^{-2}$ (blue curve) may be a result of neglecting the intricate vortex-vortex interactions.

The vortex flow behaves opposite to the Poiseuille flow of water in a pipe. Instead of moving slower towards the boundary, the vortices tend to speed up. We therefore call this type of flow *anti-Poiseuille flow*. The quantitative details of the flow behavior of course depend on the geometry and parameter

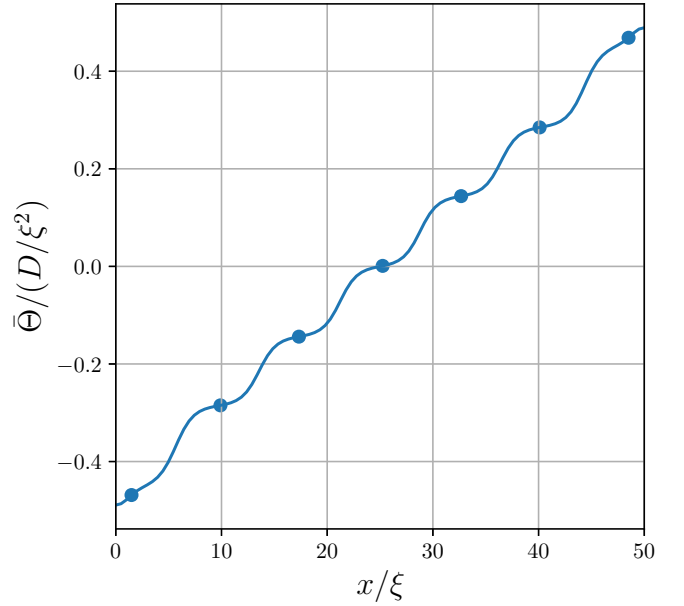


FIG. 6. Average scalar potential $\bar{\Theta}$ depending on x . The same averaging procedure and parameters as in Fig. 5 are used. The quantity $r = \Delta\bar{\Theta}$ shown by the purple squares in Fig. 5 is calculated from differences between the heights of each plateau shown. Specifically, we use the points marked by the blue dots to define r .

regime considered. To quantify this effect, we note that in our simulations the behavior can be fitted by an exponential function $v = C_0 + C_1 \cosh(C_2 \Delta x)$, where Δx is the distance from the center of a sample and $C_{0/1/2}$ are constants. Specifically, we fit the vortex speeds by $C_0 + C_1 \cosh[C_2(x - L/2)/\xi]$. In this language $C_1 < 0$ would correspond to vortices moving slower when approaching the boundary, while $C_1 > 0$ means that vortices move faster at the edges (anti-Poiseuille flow), with $|C_1|$ and $|C_2|$ quantifying the strength of the influence of the boundary.

B. Resistivity

To connect to experimentally accessible transport quantities we consider the resistances across the vortex channels $R = \Delta\bar{\Theta}/Q$, where $\Delta\bar{\Theta}$ is the difference in the scalar potential left and right of a given channel averaged over the y direction [56]. In a Bardeen-Stephen picture, that difference in the scalar potential is proportional to the number of vortices in each channel and their velocities. In Fig. 6, we show the time- and y -direction-averaged scalar potential depending on x . Since the external current is constant in our system, we can consider differences of the scalar potential $r = \Delta\bar{\Theta}$ to be directly proportional to the resistance between vortex channels. Figure 5 clearly shows that faster vortex flows (blue dots) result in proportionally higher resistance r (purple squares), in accordance with the Bardeen-Stephen picture. Following the same arguments as for the vortex velocity, we therefore find $r \propto \Delta^{-2}$.

C. Intermediate drive: Stick-slip motion

At small to intermediate sourced currents, vortex-vortex interactions become relevant and, in combination with the

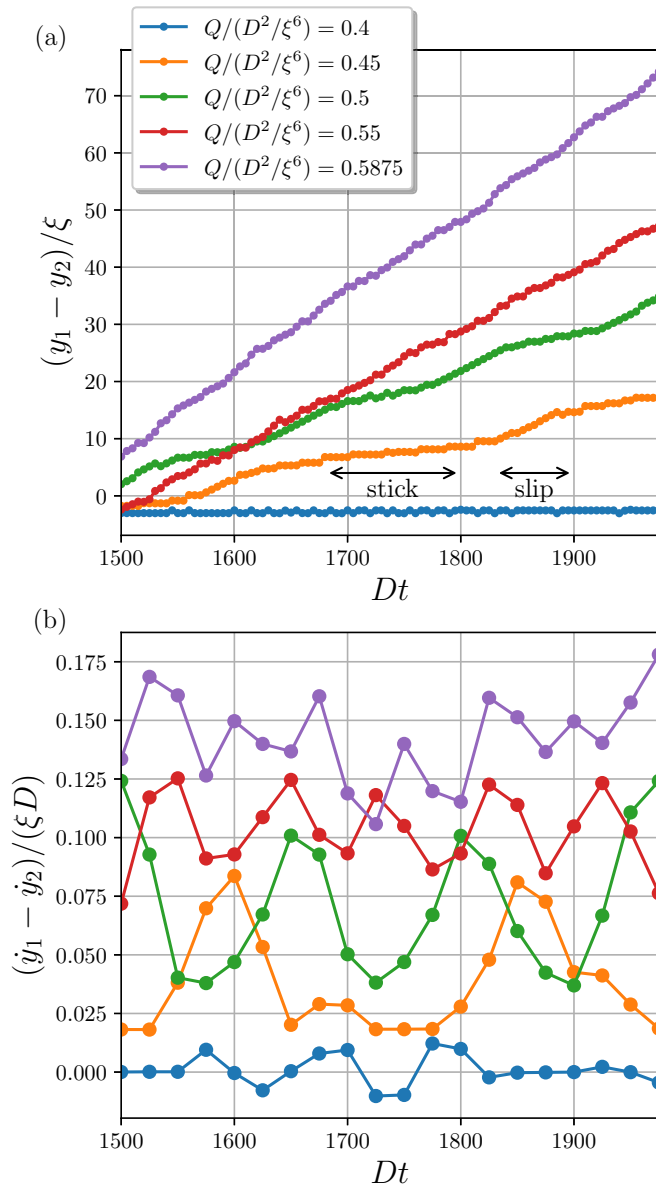


FIG. 7. (a) Differences in vortices' positions along the y direction in the leftmost y_1 and the adjacent y_2 channel as a function of time (e.g., the difference between y coordinates of the vortex marked in red and blue in Fig. 2). The periodic boundary condition is unfolded to calculate the y coordinates. (b) Corresponding time derivative of (a), namely, differences in the time-dependent velocity within the leftmost \dot{y}_1 and the adjacent \dot{y}_2 . All corresponding videos are available in the SM [53] (see also Table I in Appendix B).

local suppression of the order parameter near the boundaries, lead to an interesting time inhomogeneous stick-slip motion of the vortices. Figure 7 shows how the difference between the positions along the y direction of the leftmost y_1 and adjacent y_2 vortices evolves as a function of time Dt . For weaker drive [$Q/(D^2/\xi^6) = 0.4$] the two vortices move together [$(y_1 - y_2)/\xi$ is time independent]. For the strongest drive [$Q/(D^2/\xi^6) = 0.5875$] the two vortices move at different approximately constant velocities, but at intermediate drive a stick-slip behavior is evident, in which the relative position exhibits a series of approximately linear increases in the

difference in the positions of neighboring vortices separated by plateaus where the separation is time independent.

In Fig. 7(b) we present the difference in the corresponding time derivatives. For the smallest $Q/(D^2/\xi^6) = 0.4$, the difference in time-dependent velocities $(\dot{y}_1 - \dot{y}_2)/(\xi D)$ is almost zero at all times, meaning that the lattice moves as a whole, while for the largest $Q/(D^2/\xi^6) \gtrsim 0.55$, the velocity difference $(\dot{y}_1 - \dot{y}_2)/(\xi D)$ is essentially constant. For the intermediate Q the relative velocity alternates in time between a large value and a small value.

The times of linear increase in Fig. 7(a) with the peaks in Fig. 7(b) correspond to when the leftmost vortex passes the adjacent vortex while the plateau in Figs. 7(a) and 7(b) corresponds to the leftmost and adjacent vortices moving with the same speeds as in the small sourced current regime $Q/(D^2/\xi^6) \leq 0.4$ (see the SM, Videos 10 and 12 [53]). At each region of the linear increase in Fig. 7(a) and the peak in Fig. 7(b), a shift of the leftmost and adjacent vortex channels occurs. Or put into the language of the stick-slip phenomenology, initially, the leftmost vortex sticks to the lattice, then it accelerates and passes (slips) across the adjacent vortex, and slows down to stick again to the newly established Abrikosov lattice, which is repeated as a converged nonequilibrium stationary state. This behavior relies on the interplay between the vortex-vortex interactions and the large driving current (creating the reduced order parameter) as well as the boundary. The former tries to maintain the Abrikosov vortex lattice, while the latter two enforce the anti-Poiseuille flow. By increasing $Q/(D^2/\xi^6)$, the plateaus begin to disappear in Fig. 7(a), and in Fig. 7(b) the number of peaks increases with the decrease of the peak height, which shows that vortex-vortex interaction gradually becomes almost negligible and the speed difference between the leftmost and adjacent vortices converges to a constant. So for increasing strength of the source the stick-slip phenomenology is increasingly washed out.

V. CONCLUSION

Using time-dependent Ginzburg-Landau theory, we studied the dynamics of vortex flows in 2D superconducting thin films with an external current sourced through the sample. We found that at small sourced currents the vortex lattice moves as a whole in which all vortices move at the same velocity, while at larger sourced currents a vortex motion is assigned to channels in which vortices in channels closer to the sample edge move faster than those farther way from the sample edge. We showed that the velocity differential in the larger-current regime arises from a position dependence of the viscosity depicted as by a Bardeen-Stephen picture and expressed the equation of motion for the vortex in the channel next to the boundary. Further analysis while neglecting intricate vortex-vortex interactions yielded a simple prediction for the position-dependent vortex velocity, which demonstrates good agreement between this simple prediction and our full numerical calculations within the time-averaged analysis. The behavior of vortex flow was found to be opposite what is typical in Poiseuille-like flow; namely, the velocity of the flow increases towards the boundary. In addition, detailed real-time analysis of the vortices' motions for the larger-current regime revealed a stick-slip motion of the vortex lattice as the sourced

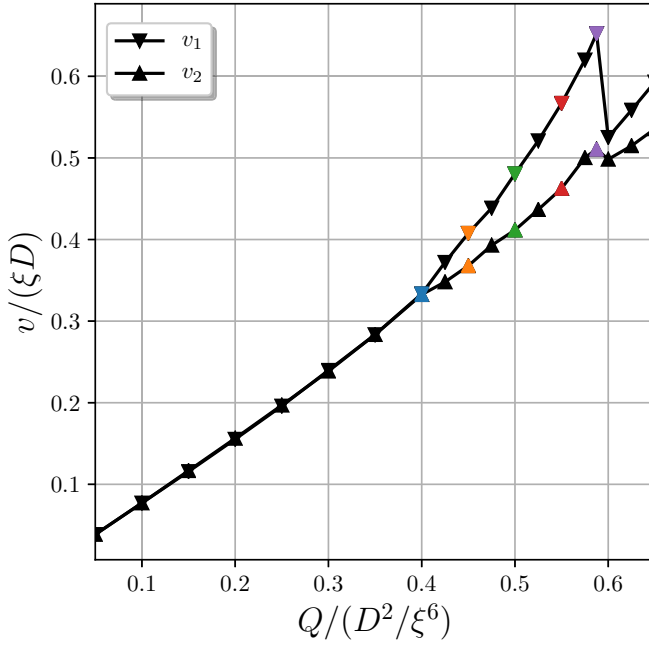


FIG. 8. The time-averaged velocities v_1 and v_2 as a function of the strength of the source term Q . The differences in the two triangles at each Q value correspond to the circles in Fig. 3.

current is increased. Initially, the vortices in the channel at the edges stick to the Abrikosov lattice; then they start to accelerate and move past their neighbors, followed by them slowing down to again stick to another reestablished Abrikosov lattice, which periodically continues as a stationary state of the system. This intricate motion relies on the interplay between the vortex-vortex interactions and the large driving current at a boundary (creating the reduced order parameter).

Experimentally, this effect may be observed by a local probe that can count the rate at which vortices cross the probe to map the vortex velocity in space along the edge. A scanning superconducting quantum interference device can be used for low Ginzburg-Landau parameter superconductors [22], $\kappa = \Lambda/\xi$ (where Λ and ξ are the penetration depth and coherent length, respectively), or one could use an ultrafast scanning tunneling microscope [57].

The numerical results presented in this paper employed a superconductor-insulator boundary. We have also investigated the case of the metal-superconductor boundary, finding the same physics (see Video 17 of the SM as an example [53], where the order parameter continuously goes to zero at the boundary as the metallic boundary would naturally create).

ACKNOWLEDGMENTS

This work was supported by the Deutsche Forschungsgemeinschaft (DFG, German Research Foundation) via RTG 1995 and Germany's Excellence Strategy - Cluster of Ex-

TABLE I. Correspondence between the video number and the parameter Q in the SM [53].

Video	Quantity	$Q/(D^2/\xi^6)$
1	$ \Delta $	0.05
2	$ \Delta $	0.10
3	$ \Delta $	0.15
4	$ \Delta $	0.20
5	$ \Delta $	0.25
6	$ \Delta $	0.30
7	$ \Delta $	0.35
8	$ \Delta $	0.40
9	$ \Delta $	0.425
10	$ \Delta $	0.45
11	$ \Delta $	0.475
12	$ \Delta $	0.5
13	$ \Delta $	0.525
14	$ \Delta $	0.55
15	$ \Delta $	0.575
16	$ \Delta $	0.5875
17	$ \Delta $	0.6
18	$ \Delta $	0.625
19	$ \Delta $	0.65

cellence Matter and Light for Quantum Computing (ML4Q) EXC 2004/1 - 390534769. A.B. and A.J.M. acknowledge support from the Center for Precision-Assembled Quantum Materials P(AQM) DMR-2011738. Simulations were performed with computing resources granted by RWTH Aachen University under Projects No. rwth0601 and No. rwth0507. The Flatiron Institute is a division of the Simons Foundation.

APPENDIX A: TIME-AVERAGED VELOCITIES v_1 AND v_2

In this Appendix, we show in Fig. 8 a plot of the individual time-averaged velocities v_1 and v_2 as a function of the strength of the source term Q . As discussed in Fig. 3, v_1 and v_2 are almost the same up to the critical value $Q \approx 0.4D^2/\xi^6$. This can also be clearly seen from Fig. 8 as the two curves overlap and show a linear increase as a function of Q . From the critical value, the slopes of the linear curves for v_1 and v_2 differ. At around $Q \approx 0.6D^2/\xi^6$, both linear curves drop because the system is reset (the number of vortex channels changes from six to four as discussed in Sec. III B). After the drop, the same $0.4 < Q/(D^2/\xi^6) < 0.6$ feature is found by linear increases as a function of Q with different slopes for v_1 and v_2 .

APPENDIX B: BRIEF EXPLANATION OF THE VIDEOS

In this Appendix, we show the correspondence between the video number and the strength of the source term Q in the SM, which is summarized in Table I.

[1] A. Abrikosov, *J. Phys. Chem. Solids* **2**, 199 (1957).

[2] J. Bardeen and M. J. Stephen, *Phys. Rev.* **140**, A1197 (1965).

[3] M. Tinkham, *Introduction to Superconductivity*, Dover Books on Physics Series (Dover Publications Inc, Mineola, New York, 2004).

- [4] M. H. Devoret and R. J. Schoelkopf, *Science* **339**, 1169 (2013).
- [5] G. Shaw, S. Blanco Alvarez, J. Brisbois, L. Burger, L. B. L. G. Pinheiro, R. B. G. Kramer, M. Motta, K. Fleury-Frenette, W. A. Ortiz, B. Vanderheyden, and A. V. Silhanek, *Metals* **9**, 1022 (2019).
- [6] W. Si, S. J. Han, X. Shi, S. N. Ehrlich, J. Jaroszynski, A. Goyal, and Q. Li, *Nat. Commun.* **4**, 1347 (2013).
- [7] U. Welp, K. Kadowaki, and R. Kleiner, *Nat. Photonics* **7**, 702 (2013).
- [8] H. Padamsee, *Supercond. Sci. Technol.* **14**, R28 (2001).
- [9] A. Gurevich and G. Ciovati, *Phys. Rev. B* **77**, 104501 (2008).
- [10] I. S. Veshchunov, W. Magrini, S. V. Mironov, A. G. Godin, J.-B. Trebbia, A. I. Buzdin, P. Tamarat, and B. Lounis, *Nat. Commun.* **7**, 12801 (2016).
- [11] I. Madan, J. Buh, V. V. Baranov, V. V. Kabanov, A. Mrzel, and D. Mihailovic, *Sci. Adv.* **4**, eaao0043 (2018).
- [12] V. Rouco, C. Navau, N. Del-Valle, D. Massarotti, G. P. Papari, D. Stornaiuolo, X. Obradors, T. Puig, F. Tafuri, A. Sanchez, and A. Palau, *Nano Lett.* **19**, 4174 (2019).
- [13] I. Tamir, A. Benyamini, E. J. Telford, F. Gorniaczyk, A. Doron, T. Levinson, D. Wang, F. Gay, B. Sacépé, J. Hone, K. Watanabe, T. Taniguchi, C. R. Dean, A. N. Pasupathy, and D. Shahar, *Sci. Adv.* **5**, eaau3826 (2019).
- [14] A.-C. Shi and A. J. Berlinsky, *Phys. Rev. Lett.* **67**, 1926 (1991).
- [15] A. E. Koshelev and V. M. Vinokur, *Phys. Rev. Lett.* **73**, 3580 (1994).
- [16] T. Giamarchi and P. Le Doussal, *Phys. Rev. Lett.* **76**, 3408 (1996).
- [17] K. Moon, R. T. Scalettar, and G. T. Zimányi, *Phys. Rev. Lett.* **77**, 2778 (1996).
- [18] N. Grønbech-Jensen, A. R. Bishop, and D. Domínguez, *Phys. Rev. Lett.* **76**, 2985 (1996).
- [19] C. Reichhardt, C. J. Olson, and F. Nori, *Phys. Rev. Lett.* **78**, 2648 (1997).
- [20] C. Reichhardt and C. J. Olson Reichhardt, *Phys. Rev. B* **81**, 100506(R) (2010).
- [21] C. Reichhardt and C. J. O. Reichhardt, *Low Temp. Phys.* **46**, 309 (2020).
- [22] L. Embon, Y. Anahory, Ž. Jelić, E. O. Lachman, Y. Myasoedov, M. E. Huber, G. P. Mikitik, A. V. Silhanek, M. V. Milošević, A. Gurevich, and E. Zeldov, *Nat. Commun.* **8**, 85 (2017).
- [23] O. V. Dobrovolskiy, D. Y. Vodolazov, F. Porrati, R. Sachser, V. M. Bezv, M. Y. Mikhailov, A. V. Chumak, and M. Huth, *Nat. Commun.* **11**, 3291 (2020).
- [24] D. Y. Vodolazov and F. M. Peeters, *Phys. Rev. B* **76**, 014521 (2007).
- [25] D. Y. Vodolazov, *Phys. Rev. B* **88**, 014525 (2013).
- [26] G. Grimaldi, A. Leo, P. Sabatino, G. Carapella, A. Nigro, S. Pace, V. V. Moshchalkov, and A. V. Silhanek, *Phys. Rev. B* **92**, 024513 (2015).
- [27] C. Reichhardt and C. J. O. Reichhardt, *Phys. Rev. B* **101**, 054423 (2020).
- [28] C. Reichhardt and C. J. O. Reichhardt, *Europhys. Lett.* **129**, 21001 (2020).
- [29] N. S. Lin, V. R. Misko, and F. M. Peeters, *Phys. Rev. Lett.* **102**, 197003 (2009).
- [30] M. C. Miguel and S. Zapperi, *Nat. Mater.* **2**, 477 (2003).
- [31] M. C. Marchetti and D. R. Nelson, *Phys. Rev. B* **59**, 13624 (1999).
- [32] R. Besseling, R. Niggebrugge, and P. H. Kes, *Phys. Rev. Lett.* **82**, 3144 (1999).
- [33] R. Besseling, P. H. Kes, T. Dröse, and V. M. Vinokur, *New J. Phys.* **7**, 71 (2005).
- [34] R. Seshadri and R. M. Westervelt, *Phys. Rev. Lett.* **70**, 234 (1993).
- [35] T. B. Mitchell, J. J. Bollinger, W. M. Itano, and D. H. E. Dubin, *Phys. Rev. Lett.* **87**, 183001 (2001).
- [36] G. Berdiyrov, K. Harrabi, F. Oktasendra, K. Gasmi, A. I. Mansour, J. P. Maneval, and F. M. Peeters, *Phys. Rev. B* **90**, 054506 (2014).
- [37] A. Andronov, I. Gordion, V. Kurin, I. Nefedov, and I. Shereshevsky, *Phys. C (Amsterdam, Neth.)* **213**, 193 (1993).
- [38] A. G. Sivakov, A. M. Glukhov, A. N. Omelyanchouk, Y. Koval, P. Müller, and A. V. Ustinov, *Phys. Rev. Lett.* **91**, 267001 (2003).
- [39] R. S. Keizer, M. G. Flokstra, J. Aarts, and T. M. Klapwijk, *Phys. Rev. Lett.* **96**, 147002 (2006).
- [40] G. R. Berdiyrov, M. V. Milošević, and F. M. Peeters, *Phys. Rev. B* **79**, 184506 (2009).
- [41] A. V. Silhanek, M. V. Milošević, R. B. G. Kramer, G. R. Berdiyrov, J. Van de Vondel, R. F. Luccas, T. Puig, F. M. Peeters, and V. V. Moshchalkov, *Phys. Rev. Lett.* **104**, 017001 (2010).
- [42] A. I. Larkin and Y. Ovchinnikov, *Sov. Phys. JETP* **41**, 960â (1975).
- [43] L. P. Gorâkov, *Sov. Phys. JETP* **9**, 1364 (1959).
- [44] A. Schmid, *Phys. Kondens. Mater.* **5**, 302 (1966).
- [45] M. Cyrot, *Rep. Prog. Phys.* **36**, 103 (1973).
- [46] D. M. Kennes and A. J. Millis, *Phys. Rev. B* **96**, 064507 (2017).
- [47] A. Benyamini, E. J. Telford, D. M. Kennes, D. Wang, A. Williams, K. Watanabe, T. Taniguchi, D. Shahar, J. Hone, C. R. Dean, A. J. Millis, and A. N. Pasupathy, *Nat. Phys.* **15**, 947 (2019).
- [48] A. Benyamini, D. M. Kennes, E. J. Telford, K. Watanabe, T. Taniguchi, A. J. Millis, J. Hone, C. R. Dean, and A. N. Pasupathy, *Nano Lett.* **21**, 583 (2021).
- [49] However, the gauge function χ cannot be fixed uniquely only by this condition for the finite-element method; that is, χ can be determined only up to a constant. Thus, we introduce another condition, $\int_S \Psi dS = 0$, where S is the entire sample domain [58,59].
- [50] G. Carapella, P. Sabatino, and G. Costabile, *J. Phys.: Condens. Matter* **23**, 435701 (2011).
- [51] P. Sabatino, G. Carapella, and G. Costabile, *Supercond. Sci. Technol.* **24**, 125007 (2011).
- [52] When vortices move out of the finite sample, critical force which overcomes any barrier is needed. For a large enough slab, such an effect will be irrelevant since the collective force of the current over all vortices is much larger than any barrier.
- [53] See Supplemental Material at <http://link.aps.org/supplemental/10.1103/PhysRevB.105.224512> for the videos.
- [54] A. Logg, K. Mardal, and G. Wells (Eds.), *Automated Solution of Differential Equations by the Finite Element Method* (Springer, Berlin, Heidelberg, 2012).
- [55] Specifically, both the real and imaginary parts of the complex order parameter $\text{Re}[\Delta]$ and $\text{Im}[\Delta]$ are set to $\sqrt{0.5} + \delta$, where δ is chosen randomly from a uniform distribution $\delta \in$

- ($-0.01, 0.01$). However, since we concentrate on analyzing the steady state, none of the general conclusions are affected by the initial conditions.
- [56] M. Machida and H. Kaburaki, *Phys. Rev. Lett.* **71**, 3206 (1993).
- [57] N. N. Khusnatdinov, Jr., T. Nagle, and G. Nunes, Jr., *Appl. Phys. Lett.* **77**, 4434 (2000).
- [58] Q. Du, *Appl. Anal.* **53**, 1 (1994).
- [59] J. Fan, B. Samet, and Y. Zhou, *Osaka J. Math.* **56**, 269 (2019).